Stabilizing Aerodynamic Dampers for Cooperative Transport of a Suspended Payload with Aerial Robots

Dong, Kaixu; Ding, Runze; Bai, Songnan; Cai, Xinyu; Chirarattananon, Pakpong

Published in:
Advanced Intelligent Systems

Published: 01/09/2023

Document Version:
Final Published version, also known as Publisher's PDF, Publisher's Final version or Version of Record

Published version (DOI):
10.1002/aisy.202300112

Publication details:
Dong, K., Ding, R., Bai, S., Cai, X., & Chirarattananon, P. (2023). Stabilizing Aerodynamic Dampers for Cooperative Transport of a Suspended Payload with Aerial Robots. *Advanced Intelligent Systems*, *5*(9), Article 2300112. https://doi.org/10.1002/aisy.202300112

ADVANCED INTELLIGENT SYSTEMS Open Access
www.advintellsyst.com

Stabilizing Aerodynamic Dampers for Cooperative Transport of a Suspended Payload with Aerial Robots

*Kaixu Dong, Runze Ding, Songnan Bai, Xinyu Cai, and Pakpong Chirarattananon**

The current paper addresses the problem of stabilizing multiple aerial robots cooperatively transporting a cable-suspended payload by an aeromechanic method. Instead of relying on global navigation satellite systems (GNSS) or vision and communication for agents to actively estimate and control the state of the multibody dynamics, lightweight air dampers to make the multiagent system inherently stable at its equilibrium state, permitting the robots to safely carry a load at a constant velocity are employed. This is achieved without additional state estimation or active correction. The proposed framework is proven stable and verified by simulations and extensive flight experiments. Lightweight mechanical dampers (under 7 g) are shown to be effective in attenuating undesired oscillations and overcoming disturbances. To this end, a team of four robots cooperatively transporting a payload over 20 m in open space is demonstrated, and three robots safely transporting a point-mass payload over a distance of 45 m outdoors. The promising outcomes highlight the benefits of the passive strategy, which demands minimal hardware components and computation to realize the sophisticated aerial transport task.

1. Introduction

With the progress in control and autonomous navigation,[1–4] aerial robots have shown promise in a wide spectrum of field applications, including cave exploration,[5] contact-based inspection,[6] and herding a flock of birds.[7] Among various uses of aerial robots, the transport of a suspended payload has gathered immense interest as its impact extends beyond the aerial delivery of packages or medical supplies.[8] The ability to carry a tool permits robots to manipulate objects,[9] aid construction,[10] or extinguish fire.[11]

To carry a payload with a single aerial robot, the payload is either grasped/fixed or hoisted. The difficulties with a fixed payload lie in achieving a stable attachment[12] and accounting for the center of mass of the payload and the resultant inertia of the combined robot-payload body, which may not be known in advance.[13,14] A tethered payload eliminates a grasping mechanism, relaxing the requirement on the shape of the object. The suspension, however, brings extra degrees of freedom.[15] Without full consideration of the multibody dynamics, the load may dynamically undergo large swings and destabilize the flight.[15,16]

Another fundamental challenge associated with the aerial transport task stems from the elevated thrust requirement, which exacerbates dramatically as the vehicle sizes reduce.[17,18] Small robots suffer from severely reduced payload capacity. As a consequence, a team of micro aerial vehicles (MAVs) can be deployed to collaboratively carry a heavier payload. However, the multiagent method inevitably brings about additional complications. In the case of a rigidly attached payload,[13,19–21] the entire structure with multiple robots may be regarded as a rigid body. At the minimum, some knowledge of mass distribution is required to realize suitable thrust allocation between different robots to stabilize flight. For a tethered payload, several robots must operate together to ensure the stability of the multibody system under the holonomic constraints imposed by the cables.

To safely and autonomously carry a suspended payload with multiple aerial robots, the task may conventionally be divided into three aspects. The first is the generation of feasible trajectories and planning. The second concerns a method to stabilize the formation, keeping each agent away from its neighbors and the payload to avoid a collision. The last aspect involves feedback and communication. As certain measurements of the state variables are needed for each robot to execute the derived control commands, the information must be available and possibly shared among agents.

Owing to the elaborated complexity, pioneering works in this topic initially focus on the trajectory generation problem. In refs. [22-24], the authors adopt a payload-centric approach to

K. Dong, R. Ding, S. Bai, P. Chirarattananon
Department of Biomedical Engineering
City University of Hong Kong
Tat Chee Avenue, Hong Kong SAR, China
E-mail: pakpong.c@cityu.edu.hk

X. Cai
Engineering Product Development Pillar
Singapore University of Technology and Design
Singapore 487372, Singapore

P. Chirarattananon
Department of Mechanical Engineering
City University of Hong Kong
Tat Chee Avenue, Hong Kong SAR, China

The ORCID identification number(s) for the author(s) of this article can be found under https://doi.org/10.1002/aisy.202300112.

DOI: 10.1002/aisy.202300112

solve the kinematics and obtain feasible equilibrium states with nonnegative cable tension. Later, differential flatness theory is applied to demonstrate that the locations of all agents can be computed from the desired pose of the payload.[25] Under the condition of fully available state feedback (from GPS or motion capture cameras, MoCap, for instance), the transport of a hoisted payload can be achieved by directly controlling the positions of the robots. Several control schemes can then be successfully implemented.[26–31]

In real-world environments, precise position feedback is not readily available. To work around the limitation, onboard cameras and inertial sensors are employed for each robot to infer the state of the cable and payload.[32–35] In ref. [32], two robots were able to carry a rigid body payload over a distance of 3.3 m. Therein, both robots acquire the relative pose of the payload through their onboard fisheye cameras, while the follower robot also tracks the leader robot in its field of view. The onboard visual odometry fulfills the feedback requirement for the transport task without relying on any communication. The approach is taken in ref.[33] is somewhat similar but without the leader–follower structure. Using a combination of perception from a monocular camera and inertial measurements, each robot estimates the state of the payload in a distributed manner. The information is then shared. As a result, the developed framework allows the payload to be transported by three robots over 30 m. In our previous work,[34,35] the leader–follower scheme was adopted for two robots to cooperatively hoist a point-mass payload. To do so, the state of the payload was estimated through the cable tension as perceived by the existing inertial sensor on the follower robot. Without directly using vision, the method allows the follower to efficiently stabilize the three-body system. Nonetheless, it remains unclear whether the vision-less approach can accommodate a system with more than two agents, owing to the observability conditions.

In this paper, we take a novel approach to realize the cooperative transport of a suspended payload. The proposed strategy is inspired by refs. [36-38], in which lightweight, aerodynamic dampers are employed for passively stabilizing the orientation and attitudes of micro aerial robots. Instead of directly estimating the state of the payload and stabilizing the coupled payload-robot dynamics as commonly accomplished previously, we substitute the feedback control process with aerodynamic-induced passive stability. By mechanically equipping the payload and robots with air dampers, as illustrated in **Figure 1** and Movie S1, Supporting Information, the system is stabilized to the intended equilibrium state without the need for robots to perform corrective maneuvers. The passive approach is entirely different from previous works in the literature. The use of aerodynamic damping entirely eliminates the need for both state estimation and control for the relative positions, as well as hardware components for high-resolution vision and demanding computation. Hence, the method is particularly appealing for small aerial robots with an already limited payload capacity.

To accomplish this, we consider a group of robots hoisting a point-mass payload traveling at a constant intended velocity. We show that, under such conditions, there exists an equilibrium state if all robots realize their respective attitude and net thrust setpoints. When deviated from this state, the load undergoes oscillations, affecting the relative positions between the agents. In this setting, we introduce a set of aerodynamic dampers—a payload stabilizer—to attenuate the undesired motion. Labeling the agents as a leader and followers, the leader can stably steer the system and change the traveling direction without communicating with the follower robots. Furthermore, to accommodate the absence of yaw or heading feedback from unreliable magnetometers, we incorporate tail dampers on the follower robots, as inspired by ref. [36]. Through the modeling of aerodynamic forces and the robot-payload dynamics, we provide an analysis based on the Lyapunov direct method to verify the stability of this passive strategy.

1.1. Aerodynamic Dampers and Passive Stabilization

Not limited to applications in aerial robots, drag from moving aerodynamic surfaces have been exploited to assist dynamic maneuvers in agile-legged robots.[39–41] In the flight domain, the use of force/moment generated by large aerodynamic surfaces for stabilization is abundant in animals and aerial vehicles. In steady forward flight, birds and conventional aircraft gain pitch stability through lifting surfaces (wings and tails) by manipulating the relative positions of the centers of gravity and lift.[42] To achieve passive attitude stability with MAVs, sizable aerodynamic surfaces are required, as demonstrated by a flapping-wing robot,[38] a samara-inspired robot,[43] and multirotors.[44,45] Thus far, aerodynamic-based stabilization has not been implemented for the cooperative aerial transport task. The use of mechanical dampers to replace sensory inputs and active computation effectively migrates the sophisticated stabilization task to mechanical structures and environmental (air) interactions by means of physical intelligence.[46] This regime makes the proposed strategy for cooperative transport distinct from previous accomplishments.[32–34]

To prevent possible confusion, it is important to clarify that the passive stability created by the air dampers in this work is entirely different from the strategy known as passivity-based control, which was developed for the cooperative aerial transport in refs. [26,28,31]. Therein, the term passivity refers to a specific approach for designing a flight controller under the conservation of energy principle. The methods in refs. [26,28,31] still rely on full knowledge of agents' location from MoCap and centralized communication, which is likely unavailable in real-world settings.

1.2. Control Autonomy of Aerial Cooperative Transport

The contribution of this work can also be seen from the perspective of flight autonomy. For a single small rotorcraft, an inertial measurement unit (IMU) and an altitude sensor (such as time-of-flight, time-of-flight [ToF], and camera) can form a minimal sensing suite for the robots to achieve sensor autonomy and realize stable flight.[47,48] Since the cooperative aerial transport task typically further demands coordination between agents to prevent a collision between agents and payload oscillations, additional sensory feedback is required for controlling the group formation on top of the flight stability at the individual level. The awareness of other robots becomes crucial, and this is conventionally provided by GPS, MoCap, or extra onboard cameras, as mentioned earlier (refer to the column "Relative positioning" in **Table 1**). The use of

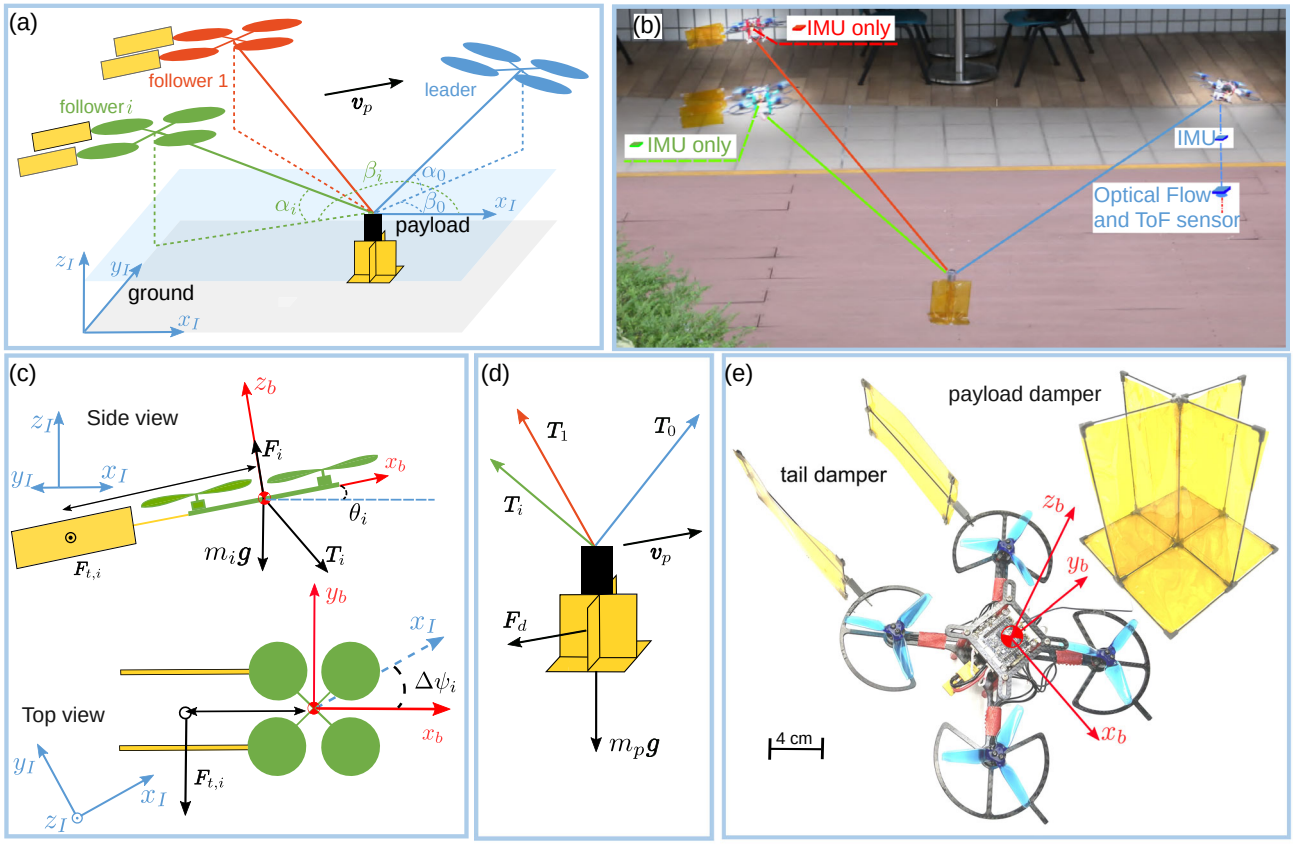

Figure 1. Overview of the aerodynamic-based stabilizing method for transporting a payload at constant velocity. a) The robots and the payload are intended to travel at a constant speed v_p. The group formation is defined by the elevation α_i and azimuth β_i angles, describing the locations of the agents with respect to the payload. The payload and tail dampers are deployed to mechanically stabilize the system. b) Photo of three robots hoisting a 161 g payload outdoors. The leader robot is equipped with a minimal set of sensors (IMU, downward-looking optical flow camera, and ToF sensor) for its own navigation. The follower robots only rely on their onboard IMUs. c) Aerodynamic force contributed by the tail dampers on the follower robot $\mathbf{F}_{t,i}$ (the drawing does not show the roll rotation). The dampers align the heading direction of the robot with the intended travel direction. Cable tension and the robot's weight are also shown. d) Force diagram of the payload illustrating the cable tension, weight, and damping force. e) Photos of the payload damper and the tail dampers on a follower robot. The dampers are fabricated from lightweight carbon fiber rod and Kapton film. The mass of the payload damper is less than 7 g. A pair of tail dampers weight is less than 4 g.

mechanical air dampers in this work totally bypasses this requirement as they physically render the multiagent dynamics passively stable. In other words, the condition for sensor autonomy of the multiagent system is readily met. As summarized in Table 1, this work differs from all previous implementations as it eliminates the reliance on the knowledge of relative positions between agents.

1.3. Content Structure

The rest of the paper is organized as follows. Section 2 provides an overview of the cable-suspended payload system, with the introduction of aerodynamic stabilizers and flight strategy. The dynamic equations and aerodynamic forces are provided in Section 3. Section 4 describes the equilibrium states and associated conditions for asymptotic stability. In Section 5, we evaluate the performance of the passive strategy through numerical simulation and extensive flight experiments, including an open-space flight with four robots and a long-distance outdoor flight with three robots. Lastly, conclusions and discussions are presented in Section 6.

2. System Overview

We consider a system consisting of several quadcopters transporting one suspended point-mass payload cooperatively with the help of aerodynamic dampers (Figure 1). The robots are designated as one leader and n followers. As defined in ref. [49], the leader may be equipped with sensors for endowing the robot with the ability to navigate and lead other robots outdoors (in this work, we incorporate an optical flow camera and a ToF sensor). However, no sensing device is required for stabilizing the payload and flight formation. For the followers, the only sensors needed for them to stabilize their flight and the payload is their onboard IMUs. Tail dampers can be optionally deployed on the follower robots in the absence of reliable feedback from onboard magnetometers for stabilizing the heading direction. Despite the

Table 1. Implementation methods for realizing aerial cooperative transport.

References	Communication	Relative positioning	Flight distance	Environment	Number of robots
This work	×	×	45 m/20 m	Outdoor/open space	3/4
Xie et al.[35]	×	IMU-based estimation	20 m	Outdoor	2
Tagliabue et al.[20]	×	Onboard vision[b)]	8 m	Outdoor	2
Li et al.[33]	Agent-to-agent[a)]	Onboard vision[b)]	31 m	Indoor	3
Gassner et al.[32]	×	Onboard vision[b)]	3.3 m	Indoor	2
Geng et al.[29]	Centralized	MoCap/GPS	5 m/2 m	indoor/outdoor	4
Zhang et al.[54]	Centralized and agent-to-agent[a)]	GPS	120 m	Outdoor	3
Klausen et al.[55]	Centralized	GPS	–	–	3
Ritz et al.[56]	Centralized	MoCap	–	–	6
Mohammad et al.[28]	Centralized	MoCap	6 m	Indoor	3
Fink et al.[23]	Centralized	MoCap	3.1 m	Indoor	3
D'antonio et al.[30]	Centralized	MoCap	3.6 m	Indoor	2
Liang et al.[57]	Centralized	MoCap	–	–	2

[a)]All robots broadcast their estimates of the formation to others. [b)]Here, the onboard vision refers to the use of vision for coordination between agents only, not for navigation.

name, in this context, the leader does not play a centralized role in stabilizing the system such that a failure of the leader to guide the followers to the desired traveling direction would not catastrophically destabilize the formation. In this section, we first describe the kinematics imposed by the cables and introduce the aerodynamic dampers, which are integral to the proposed passive stabilization method. Then, the flight strategy is explained.

2.1. Formation and Coordinate Frames

Figure 1a provides an overview of the proposed system with only two followers shown ($n = 2$). The inertial frame is defined as $\{x_I, y_I, z_I\}$, assumed to be stationary with respect to the ground or still air. An index i is adopted to identify $n + 1$ agents. For the leader $i = 0$ while $i \in \{1, 2, \cdots, n\}$ for the followers. We let l_i be the length of the cable between the point-mass payload and the *ith* robot. Defining $\mathbf{p}_p = [x_p, y_p, z_p]^T$ and $\mathbf{p}_i = [x_i, y_i, z_i]^T$ to be the positions of the payload and the robots in the inertial frame and assuming the cables are always taut, the holonomic constraints are given by the following equation

$$\|\mathbf{p}_i - \mathbf{p}_p\| = l_i \tag{1}$$

We use elevation $\alpha_i \in [0, \pi/2]$ and azimuth $\beta_i \in (-\pi, \pi]$ angles to describe the direction of the ith agent with respect to the payload as measured in the inertial frame, as presented in Figure 1a. In the vector form, Equation (1) is expressed as follows

$$\mathbf{p}_i - \mathbf{p}_p = l_i \mathbf{q}_i \tag{2}$$

where

$$\mathbf{q}_i = [\cos\alpha_i \cos\beta_i \ \cos\alpha_i \sin\beta_i \ \sin\alpha_i]^T \tag{3}$$

is a unit vector representing the cable direction. The goal of the task is for the robots and the payload to travel at constant velocity ν_p. We adopt $\mathbf{e}_1$, $\mathbf{e}_2$, and $\mathbf{e}_3$ as 3×1 basis vectors for the rest of the manuscript.

2.2. Aerodynamic Dampers

To make use of aerodynamic forces to passively stabilize the formation such that all robots maintain their velocity ν_p with minimal sensing and control requirements, an omnidirectional damper shown in Figure 1e is attached to the payload. Constructed from three perpendicular surfaces, as motivated by the design in refs. [37,38], the damping force is induced when the damper translates in any direction with respect to still air. For each follower, a pair of tail dampers in Figure 1e, similar to those present in refs. [36,39-41], may be optionally attached to the rear of the robot. Taking after the implementation in ref. [36], they are designed to create yaw torque to reorient the robot when the orientation is misaligned with the intended traveling direction ν_p. This eliminates the need for precise yaw feedback for heading control.

2.3. Cooperative Flight Strategy

To realize the aerial transport task with multiple robots through the use of dampers, the leader is nominally responsible for determining the setpoint velocity of the group (ν_p in Figure 1a). With only onboard inertial sensors assumed for the followers, they are only required to realize the attitude setpoint, together with the desired level of total thrust force. As the cables are mounted near the center of mass of each robot, creating no torque, it is reasonable to assume the attitude of the followers is precisely controlled by the low-level flight controller that actively realizes the attitude setpoint and minimizes the rotational rate. This leaves only the translational dynamics to be stabilized. As elaborated in the subsequent sections, the contribution from payload dampers ensures that the multirobot system stabilizes to the configuration where every robot travels at the same constant velocity ν_p and

maintains their relative positions. In addition, tail dampers may be deployed to deal with situations where the yaw (heading) feedback from built-in magnetometers is unavailable.

3. Dynamic Model and Influence of Aeromechanic Stabilizers

In this section, the dynamics of the multirobot system are first derived. Then, the contribution of the aerodynamic dampers to the dynamics is evaluated.

3.1. Translational Dynamics

The dynamics of each robot, including the leader and followers, are established in the inertial frame shown in Figure 1. In addition to the weight and thrust, each robot is subject to the cable tension T_i and the damping force attributed by the tails, as seen in Figure 1c. Therefore, the equations of motion are given by the following equation

$$m_i\ddot{\mathbf{p}}_i = \mathbf{F}_i - m_i g\mathbf{e}_3 - T_i\mathbf{q}_i + \mathbf{F}_{\mathrm{t},i} \tag{4}$$

where $m_i g$ denotes the weight of the robot, $\mathbf{F}_i$ is the collective thrust generated by each robot, T_i is the tension of the cable connecting the payload and the agent, and $\mathbf{F}_{\mathrm{t},i}$ stands for the aerodynamic forces created by the tail dampers when they are present, otherwise, $\mathbf{F}_{t,i} = 0$. Since the axis of the propeller is aligned with the yaw axis of the robot (z_b in Figure 1c), the propelling thrust $\mathbf{F}_i$ of each robot in Equation (4) maybe rewritten using the rotation matrix $\mathbf{R}_i$ as $\mathbf{F}_i = F_i\mathbf{R}_i\mathbf{e}_3$ for $\mathbf{F}_i = \|\mathbf{F}_i\|$. As previously mentioned, the low-level attitude controller ensures the desired value of $\mathbf{F}_i$ is realized.

The dynamics of the payload are governed by the pulling forces from n cables and the damping from the omnidirectional stabilizer $\mathbf{F}_\mathrm{d}$, as depicted in Figure 1d.

$$m_\mathrm{p}\ddot{\mathbf{p}}_\mathrm{p} = \sum_{i=0}^{n} T_i\mathbf{q}_i - m_\mathrm{p}g\mathbf{e}_3 + \mathbf{F}_\mathrm{d} \tag{5}$$

where m_p is the payload's mass. In comparison to the stabilizers, the contribution of aerodynamic damping from the body of the robots and the payload is assumed negligible.

Furthermore, regarding the cable tension as internal forces, Equation (4) and (5) combine into the following equation

$$\sum_{i=0}^{n} m_i\ddot{\mathbf{p}}_i + m_\mathrm{p}\ddot{\mathbf{p}}_\mathrm{p} = \sum_{i=0}^{n}(\mathbf{F}_i\mathbf{R}_i\mathbf{e}_3 - m_i g\mathbf{e}_3 + \mathbf{F}_{\mathrm{t},i}) - m_\mathrm{p}g\mathbf{e}_3 - \mathbf{F}_\mathrm{d} \tag{6}$$

which collectively describes the translation of the center of mass of the system.

3.2. Aerodynamic Damping

The drag generated by the aerodynamic surfaces is often modeled to be quadratic to the projected air speed and orthogonal to the surface.[39,40,50,51] Since the payload stabilizer consists of three orthogonal surfaces, the total aerodynamic damping becomes approximately isotropic. The drag force is directly dependent on the relative air velocity. That is

$$\mathbf{F}_\mathrm{d} = -\frac{1}{2}\rho A_\mathrm{d} C_\mathrm{d}\,\mathrm{diag}(|\dot{\mathbf{p}}_\mathrm{p}|)\dot{\mathbf{p}}_\mathrm{p} \tag{7}$$

where ρ is the air density, A_d is an effective area, and $C_\mathrm{d} = 2$ is the drag coefficient for a flat plate.[51] Note that in Equation (7), $|\dot{\mathbf{p}}_\mathrm{p}| \in \mathrm{R}^3$ does not refer to the Euclidean norm, but it returns absolute values of elements in $\dot{\mathbf{p}}_\mathrm{p}$.

For flat tail dampers, the aerodynamic force, or $\mathbf{F}_{\mathrm{t},i}$ in Equation (5), is normal to the surface (parallel to a unit vector $\mathbf{e}_{\mathrm{t},i}$ in the body frame in Figure 1c) and quadratically proportional to the perceived air speed attributed to the translation, $\dot{\mathbf{p}}_i^\mathrm{T}\mathbf{R}_i\mathbf{e}_{\mathrm{t},i}$, in the direction perpendicular to the damper, $\mathbf{R}_i\mathbf{e}_{\mathrm{t},i}$.[50] The contribution from the rotational rate is minimal as the attitude (and angular rate) of the robot is directly controlled. Hence

$$\mathbf{F}_{\mathrm{t},i} = -\frac{1}{2}\rho A_\mathrm{t} C_\mathrm{d}(\dot{\mathbf{p}}_i^\mathrm{T}\mathbf{R}_i\mathbf{e}_{t,i})|\dot{\mathbf{p}}_i^\mathrm{T}\mathbf{R}_i\mathbf{e}_{\mathrm{t},i}|\mathbf{R}_i\mathbf{e}_{\mathrm{t},i} \tag{8}$$

In the meantime, the damping force also brings about the damping torque about the follower's yaw axis. Approximating the aerodynamic center of pressure to be at the geometric center of the two tails located at a distance d_t from the center of mass of the robot on the leeward side, we have

$$\tau_{\mathrm{t},i} = -d_t\mathbf{e}_2^\mathrm{T}\mathbf{R}_i^\mathrm{T}\mathbf{F}_{t,i} = \frac{1}{2}\rho A_\mathrm{t} C_\mathrm{d} d_\mathrm{t}(\dot{\mathbf{p}}_i^\mathrm{T}\mathbf{R}_i\mathbf{e}_{\mathrm{t},i})|\dot{\mathbf{p}}_i^\mathrm{T}\mathbf{R}_i\mathbf{e}_{\mathrm{t},i}| \tag{9}$$

When the tail dampers are not deployed, $\mathbf{F}_{\mathrm{t},i}$ and $\tau_{t,i}$ are all zero.

4. Aerodynamic Damping for Stabilization

In this section, we first inspect the consequence of the proposed flight strategy (i.e., only requiring the robots to use IMU feedback to maintain their thrust vectors). This results in an equilibrium state with all robots traveling at the same velocity ν_p. With only the payload dampers, the equilibrium state is shown as asymptotically stable, as any deviating motion is aerodynamically damped. In the second part, we include tail dampers on the robot to allow the multiagent system to reach the consensus velocity ν_p even when the followers are deprived of yaw feedback (knowledge of the heading direction).

4.1. Equilibrium Conditions

To gain some initial insights into the conditions for stable payload transport, we first inspect the equilibrium conditions and employ the notation to indicate the equilibrium state. The scenario of interest is when all robots and the payload, with the payload damper but without tail dampers, are traveling at a constant horizontal velocity $\dot{\mathbf{p}}_i, \dot{\mathbf{p}}_\mathrm{p} = \nu_\mathrm{p}$ with respect to the still air $\ddot{\mathbf{p}}_i, \ddot{\mathbf{p}}_\mathrm{p} = 0$.

Based on the combined translational dynamics in Equation (6), the equilibrium conditions are obtained when the forces on the right-hand side of Equation (6) are balanced.

Without tail dampers ($\mathbf{F}_{t,i} = 0$), the vertical component of Equation (6) becomes the following equation

$$0 = \sum_{i=0}^{n} \mathbf{e}_3^{\mathrm{T}}(\overline{\mathbf{F}}_i - m_i g) - m_{\mathrm{p}} g - \rho A_{\mathrm{d}} \mathbf{e}_3^{\mathrm{T}} \mathrm{diag}(|\nu_{\mathrm{p}}|)\nu_{\mathrm{p}} \tag{10}$$

which is satisfied when the sum of the vertical component of the propelling thrusts from n robots is equal to the combined weight and the vertical component of the damping force. Concurrently, the horizontal components of Equation (6) turn to the following equation

$$0 = \sum_{i=0}^{n} \mathbf{e}_{1,2}^{\mathrm{T}} \overline{\mathbf{F}}_i - \rho A_d \mathbf{e}_{1,2}^{\mathrm{T}} \mathrm{diag}(|\nu_{\mathrm{p}}|)\nu_{\mathrm{p}} \tag{11}$$

in which $\mathbf{e}_{1,2}^{\mathrm{T}}$ refers to either $\mathbf{e}_1^{\mathrm{T}}$ or $\mathbf{e}_2^{\mathrm{T}}$. The outcome states that the equilibrium transport velocity ν_{p} is determined by the total propelling thrusts and the masses of the agents and payload. This ν_{p} exists so long as Equation (10) and (11) are satisfied. In equilibrium, the sum of the thrust vectors must be equal to the weight of all robots and the damping force generated by the damper.

4.2. Equilibrium Configuration

Given the equilibrium conditions captured by Equations (12) and (13), we can either (i) start with the desired configuration of the system $\overline{\mathbf{q}}_i$ and solve for the needed thrust vector setpoints $\overline{\mathbf{F}}_i$'s; or (ii) compute the resultant system's configuration from the robots' thrust vectors. These are referred to as the direct and inverse problems in ref. [23].

4.2.1. Direct Problem

Given the desired traveling velocity ν_{p} and the system's formation $\overline{\mathbf{q}}_i$'s (this could be in terms of elevation α_i and azimuth β_i angles), we use Equation (5) to determine the equilibrium state of the payload. This yields

$$\sum_{i=0}^{n} \overline{T}_i \overline{\mathbf{q}}_i - m_{\mathrm{p}} g \mathbf{e}_3 - \rho A_{\mathrm{d}} \mathrm{diag}(|\nu_{\mathrm{p}}|)\nu_{\mathrm{p}} = \mathbf{0} \tag{12}$$

The feasible solution for T_i exists for the case of two agents ($n = 1$) only when they are positive (the cable is taut) and can satisfy $\boldsymbol{e}_{1,2}^{\mathrm{T}}(\overline{T}_0\overline{\mathbf{q}}_0 + \overline{T}_1\overline{\mathbf{q}}_1) = \rho A_{\mathrm{d}} \mathrm{diag}(|\nu_{\mathrm{p}}|)\mathbf{e}_{1,2}^{\mathrm{T}}\nu_{\mathrm{p}}$ and $\boldsymbol{e}_3^{\mathrm{T}}(\overline{T}_0\overline{\mathbf{q}}_0 + \overline{T}_1\overline{\mathbf{q}}_1) = \rho A_{\mathrm{d}} \mathrm{diag}(|\nu_{\mathrm{p}}|)\mathbf{e}_3^{\mathrm{T}}\nu_{\mathrm{p}} + m_{\mathrm{p}} g \mathbf{e}_3$. When three agents are involved, and the vectors $\boldsymbol{q}_i$ are linearly independent, there is likely a unique solution for $\overline{T}_i > 0$'s. When $n > 2$ or more than three robots are deployed, multiple solutions may exist and can be chosen from the method of least squares or other optimization routines.[23,52]

Once the cable tensions $\overline{T}_i$ are known, we resort to Equation (4) to evaluate the nominal thrust vector $\overline{\mathbf{F}}_i$ for each tailless robot in equilibrium

$$\overline{\mathbf{F}}_i - m_i g \mathbf{e}_3 - \overline{T}_i \overline{\mathbf{q}}_i = \mathbf{0} \tag{13}$$

In practice, $\overline{\mathbf{F}}_i$ is realized by directly controlling the attitude and thrust magnitude of the robot as $\overline{\mathbf{F}}_i = \overline{\mathbf{F}}_i \overline{\mathbf{R}}_i \mathbf{e}_3$.

4.2.2. Inverse Problem

Given the thrust vectors $\overline{\mathbf{F}}_i$, the traveling velocity ν_{p} can be found from the equilibrium conditions in Equations (10) and (11). The cable tension vector for each robot $\overline{T}_i\overline{\mathbf{q}}_i$ is then deduced from Equation (13). This allows both the system's formation $\overline{\mathbf{q}}_i$ and the tension $\overline{T}_i$ to be computed.

The finding implies that when the attitude setpoint $\mathbf{R}_i$ is not correctly realized, resulting in a different thrust vector $\overline{\mathbf{F}}_i$, the equilibrium system velocity ν_{p}, and the system's configuration $\overline{\mathbf{q}}_i$ are simply shifted. Similarly, constant disturbances lead to a change in the velocity ν_{p} without directly destabilizing the system, as detailed in Note 1, Supporting Information. The behavior renders the system robust to modeling and control errors.

4.2.3. Extension of the Inverse Problem for Navigation without Communication

In practice, we can use the leader to change the equilibrium velocity of the system ν_{p} (both magnitude and direction) without changing the thrust and attitude setpoints of the followers ($\overline{\mathbf{F}}_i, i \in \{1, 2, \ldots, n\}$). This means the leader can direct the robots to the desired direction without any interagent communication.

To do so, we resolve Equation (12) using the previous values of $\overline{T}_i\overline{\mathbf{q}}_i$ for $i \in \{1, \cdots, n\}$ and recalculate $\overline{T}_0\overline{\mathbf{q}}_0$ according to the updated velocity ν_{p}. Subsequently, an updated thrust of the leader $\overline{\mathbf{F}}_0$ is obtained from Equation (13). In short, only the attitude and thrust setpoints of the leader are changed to alter the group velocity. There is no need for agents to communicate to change the traveling direction.

4.3. Payload Damper-Induced Stability

Next, we demonstrate that the identified equilibrium state is asymptotically stable, thanks to the damping force provided by the payload dampers. To begin, we introduce a Lyapunov candidate function

$$V = V_1(\mathbf{p}_{\mathrm{p}}, \mathbf{p}_i) + V_2(\dot{\mathbf{p}}_{\mathrm{p}}, \dot{\mathbf{p}}_i) \tag{14}$$

with the first term related to the potential energy and the second term inspired by the translational kinetic energy. That is

$$V_1 = m_{\mathrm{p}} g \mathbf{p}_{\mathrm{p}}^{\mathrm{T}} \mathbf{e}_3 + \sum_{i=0}^{n} m_i g \mathbf{p}_i^{\mathrm{T}} \mathbf{e}_3 - \sum_{i=0}^{n} \mathbf{p}_i^{\mathrm{T}} \overline{\mathbf{F}}_i + \rho A_{\mathrm{d}} \mathbf{p}_{\mathrm{p}}^{\mathrm{T}} \mathrm{diag}(|\nu_{\mathrm{p}}|)\nu_{\mathrm{p}} + \gamma \tag{15}$$

$$V_2 = \frac{1}{2} m_{\mathrm{p}} (\dot{\mathbf{p}}_{\mathrm{p}} - \nu_{\mathrm{p}})^{\mathrm{T}} (\dot{\mathbf{p}}_{\mathrm{p}} - \nu_{\mathrm{p}}) + \sum_{i=0}^{n} \frac{1}{2} m_i (\dot{\mathbf{p}}_i - \nu_{\mathrm{p}})^{\mathrm{T}} (\dot{\mathbf{p}}_i - \nu_{\mathrm{p}}) \tag{16}$$

where $\gamma = \sum_{i=0}^{n} l_i \| m_i g \mathbf{e}_3 - \overline{\mathbf{F}}_i \|$ is a constant included to ensure that $V_1 \geq 0$ (see Note 2, Supporting Information). V_2 is positive definite and radially unbounded as it is quadratic. Consequently, V is minimized to zero only when the system is in equilibrium.

To verify the stability of the system, we evaluate the time derivative of V (refer to Note 3, Supporting Information for the derivation)

$$\dot{V} = -\rho A_d(|\dot{\mathbf{p}}_p - \nu_p|)^T(|\mathrm{diag}(|\dot{\mathbf{p}}_p|)\dot{\mathbf{p}}_p - \mathrm{diag}(|\nu_p|)\nu_p|) \tag{17}$$

which is strictly negative when $\dot{\mathbf{p}}_p \neq \nu_p$ and only zero when $\dot{\mathbf{p}}_p = \nu_p$. Based on the translational dynamics, the condition $\dot{\mathbf{p}}_p = \nu_p$ necessitates $\dot{\mathbf{p}}_i = \nu_p$. Therefore, the system is asymptotically stable according to LaSalle's invariance principle. In other words, any velocity errors would be passively attenuated by the payload dampers, resulting in a stable formation for the cooperative transport.

4.4. Tail Dampers for Coordination without Yaw Feedback

In the case of unavailable yaw feedback from an onboard magnetometer, such as indoor environments or the presence of magnetic interference, the controller on each robot is unable to fully realize the desired attitude $\mathbf{R}_i$ and, subsequently, the nominal thrust vector $\mathbf{F}_i = \mathbf{F}_i\mathbf{R}_i\mathbf{e}_3$. In such scenarios, the conclusion drawn from the inverse problem indicates that the formation velocity ν_p is impacted. The tail dampers are introduced on the follower robots to alleviate the navigation problem without yaw feedback by enabling the robots to reach a consensus velocity primarily dictated by the leader.

To illustrate, we formulate the rotation matrix with sequential pitch θ, roll ϕ, and yaw ψ rotations: $\mathbf{R}_i = \mathbf{R}_{z,i}(\psi_i)\mathbf{R}_{x,i}(\phi_i)\mathbf{R}_{y,i}(\theta_i)$, such that the actual rotation matrix may be affected by a yaw error $\mathbf{R}_z(\Delta\psi)$ when yaw feedback is inaccurate (i.e., drifting because only the yaw rate is minimized) while pitch and roll angles are still correctly controlled. This means

$$\mathbf{R}_i = \mathbf{R}_{z,i}(\Delta\psi_i)\mathbf{R}_{z,i}(\psi_i)\mathbf{R}_{x,i}(\phi_i)\mathbf{R}_{y,i}(\theta_i) = \mathbf{R}_{z,i}(\Delta\psi_i)\overline{\mathbf{R}}_i \tag{18}$$

which affects the horizontal component of the thrust vector

$$\mathbf{F}_i = \mathbf{F}_i\mathbf{R}_{z,i}(\Delta\psi_i)\overline{\mathbf{R}}_i\mathbf{e}_3 = \mathbf{R}_{z,i}(\Delta\psi_i)\overline{\mathbf{F}}_i \tag{19}$$

As per Equation (11) and subsequent stability analysis, yaw errors shift the equilibrium transport velocity ν_p, but they do not directly affect the stability of the formation.

Tail dampers are attached to follower robots to mitigate the influence of yaw errors. They are mounted on the followers with their surfaces normal $\mathbf{e}_{t,i}$ orthogonal to the intended travel direction ν_p, such that the drag force and torque described by Equations (8) and (9) vanish when $\Delta\psi_i = 0$ and $\dot{\mathbf{p}}_i$ is approximately ν_p as $\nu_p^T\overline{\mathbf{R}}_i\mathbf{e}_{t,i} = 0$. On the other hand, any yaw error, rendering $\mathbf{R}_i \neq \overline{\mathbf{R}}_i$, brings about a restoring torque

$$\begin{aligned}\tau_{t,i} &= \frac{1}{2}\rho A_t C_d d_t(\nu_p^T\mathbf{R}_{z,i}(\Delta\psi_i)\overline{\mathbf{R}}_i\mathbf{e}_{t,i})|\nu_p^T\mathbf{R}_{z,i}(\Delta\psi_i)\overline{\mathbf{R}}_i\mathbf{e}_{t,i}| \\ &= -\frac{1}{2}\rho A_t C_d d_t\|\nu_p\|^2|\sin\Delta\psi_i|\sin\Delta\psi_i\end{aligned} \tag{20}$$

for $-\pi/2 < \Delta\psi_i < \pi/2$. To show that this aerodynamic torque stabilizes the yaw error, we consider the 1D equation of motion describing the rotation of the robot about the vertical axis (as pitch and roll angles are controlled). We let $I_{\psi,i}$ be the moment of inertia of the ith follower in the respective state. Hence,

$$I_{\psi,i}\Delta\ddot{\psi}_i = -k_{\psi,i}\Delta\dot{\psi}_i - \frac{1}{2}\rho A_t C_d d_t\|\nu_p\|^2|\sin\Delta\psi_i|\sin\Delta\psi_i \tag{21}$$

where the term $-k_{\psi,i}\Delta\dot{\psi}_i$ reflects the rate damping commanded by the onboard controller. As detailed in Note S4, Supporting Information, the proportional-integration-derivative (PID)-like structure of Equation (21) means the yaw error dynamics is asymptotically stable for $-\pi/2 < \Delta\psi_i < \pi/2$. That is, the combination of tail dampers and active gyro-dependent yaw rate control is an effective substitute of the active yaw angle feedback for correcting and aligning the traveling direction of the robots.

Remark that before the yaw errors converge, the forces induced by the tail dampers described by Equation (8) may affect the translational dynamics as disturbances. However, this damping is bounded and quickly decreases to zero, posing no adverse consequence on the stability, as verified in the simulation and flight experiments below.

5. Numerical and Experimental Validation

The stability analysis of the system suggests that the relative positions among the agents are stabilized by the payload dampers, and the yaw orientation of the followers can be regulated by the tail dampers when magnetometer feedback is unavailable. To fully validate the proposed strategy, we carried out simulation and flight experiments in various settings, such as in indoor environments as well as in open spaces.

5.1. Practical Consideration

The proposed strategy and the associated stability analysis guarantee that when all the robots execute the desired attitude and thrust commands, they realize the transport velocity ν_p and the formation defined by the elevation and azimuth angles. This theoretically ensures the stability of the system. Nevertheless, it does not correct for any possible drift in the altitude nor guarantee the actual traveling velocity.

Therefore, in the implementation, the leader is responsible for maintaining the target altitude. To do so, we directly control the altitude of the leader. Moreover, the leader may be responsible for the group navigation by attempting to regulate its flight velocity to match the target velocity ν_p. In an ideal scenario with no modeling errors or disturbances, the commands executed by the leader robot would be identical to the nominal thrust vector $\boldsymbol{F}_0$. In practice, the actual command may deviate slightly, but the strategy allows the robots to collectively navigate. The robot-payload system is expected to remain stable despite some minor differences in the implementation details.

5.2. Robots and Experimental Setup

5.2.1. Leader and Follower Robots

Robots used in the experiments were constructed from Crazyflie Bolt (Bitcraze) as the flight control boards. The mass of the leader is $m_0 = 214$ g, whereas each follower weighs 219 g without the tail dampers. As described, onboard IMUs (without magnetometers) are the only sensors for the followers to regulate their attitudes. For the leader, an integrated optical flow and ToF sensor (Flow Deck v2, Bitcraze) was employed to allow the robot to travel at constant altitude and speed when leading the

formation in open-space experiments. One laptop was used as the ground station for communication (initiating and ending the experiments).

5.2.2. Thrust Mapping

Part of the developed strategy (indicated by Equation (13)) requires each follower to generate a specific magnitude of thrust $\mathbf{F}_i$ and maintain a particular attitude (roll and pitch). To accomplish this, we first identified the mapping between the driving commands of the low-level onboard controller (Crazyflie, Bitcraze) and the propelling force. A benchtop test with a load cell (Nano 17, ATI) was used for creating the thrust mapping. The detailed method is described in ref. [53].

5.2.3. Onboard Flight Controller

For indoor flights, we employed feedback from the motion capture system (MoCap) to directly control the position of the leader to restrict the robots in the confined space and record the ground truth data for all the agents in the formation (all the robots and the payload). In open space (both indoors and outdoors), the velocity and altitude of the leader were regulated using feedback from the onboard optical sensors. In both settings, the followers realized the desired attitude and collective thrust magnitude via a PID attitude controller, making use of the identified thrust model.

5.2.4. Aerodynamic Dampers

Dampers are preferred to be lightweight with large aerodynamic surfaces. They are made from carbon fiber tubes (1 mm in diameter) and Kapton sheet (25 μm in thickness), as presented in Figure 1d. The payload stabilizer weighs 6.7 g, consisting of three orthogonal 14×14 cm surfaces for creating omnidirectional damping forces. A pair of 13×7 cm tail dampers weighs 3.1 g. The effective areal density of the payload and tail dampers are 11 and 17 mg cm^{-2}, significantly lower than the 108 mg cm^{-2} density of the 5×5 cm damper in ref. [39]. When mounted on the followers, as shown in Figure 1d, the center of pressure is $d_t = 11.5$ cm away from the center of mass of the robots, and the gross weight of the followers becomes $m_1, m_2, m_3 = 222$ g.

5.2.5. Flight Area

Indoor experiments were conducted in a flight arena equipped with the MoCap (NaturalPoint, OptiTrack Prime 13w) for providing ground truth data, yaw feedback, and controlling the position of the leader. For experiments in open space, the positions of the robots and the payload were triangulated (postprocessed) from videos recorded by two fixed cameras. This requires manual labeling of the robots and the payload in the videos. The detailed procedure can be found in ref. [50]. The outcomes are sufficiently precise to generate the trajectory plots of the entire formation. Dummy masses $m_p = 111$, 161, 211 g (including the 6.7 g dampers) were employed as payloads for experiments with two, three, and four robots, respectively, making the ratio of the payload weight to the weight of all robots be ≈25%. The length of each cable (l_0, l_1, l_2, l_3) was 1.1 m, long enough for the wake generated by the robots not to visibly influence the dampers attached to the payload.

5.3. Numerical Simulation

Before conducting actual flight experiments, we carried out computational simulations to verify the stability of the framework. The numerical method permits the convergence of the Lyapunov function defined by Equation (17) to be directly verified.

The simulated scenario concerns one leader and two follower robots. Physical parameters used correspond to the actual experimental system described in Section 5.2. For calculating the damping forces, $\rho = 1.2$ kg m^{-3}, A_d is nominally 196 cm^2 and A_t is 2×90 cm^2 (a pair). To inspect the influence of these coefficients on the convergence rate, we also tested $A_d = 0, 98, 392$ and $A_t = 0, 90, 360$ cm^2 (half and double the nominal sizes).

Without loss of generality, $\nu_p = \nu_p \mathbf{e}_1$ was chosen, with the speed $\nu_p = 1.5$ m s^{-1}. The equilibrium configuration (setpoints), or $\mathbf{q}_i$, was prescribed in terms of elevation and azimuth angles, as listed in **Table 2**. The initial state was offset from the equilibrium state by significant margins. Two sets of simulations were performed, without (**Figure 2**a) and with (Figure 2b) tail dampers on the followers. Without the tail dampers, the yaw angles were controlled $\Delta\psi_i = 0$, representing scenarios with reliable magnetometer feedback. With the tail dampers, the followers started with initial yaw errors, as listed in Table 2.

Figure 2 illustrates the trajectory of the robots as angles over the period of 100 s. It can be seen that, in the absence of tail dampers, the yaw angles remain unchanged throughout as the robots were subject to zero net torque. All azimuth and elevation angles kept oscillating without a decreasing trend. This is because, without damping, the energy in the system was conserved (as $\mathbf{F}_i$'s are constant and can be regarded as conservative forces). In contrast, with the increasing values of A_d and A_t (Figure 2b–d), all state angles converged to the equilibrium values at increasing rates. The cable angles responded similarly to an underdamped system, whereas the yaw angles in Figure 2b converged noticeably faster. The plots of the Lyapunov function in Figure S1, Supporting Information, verify the convergence suggested by Equation (17) for both sets of the simulation. The convergence rate is highly dependent on the damping coefficients mainly determined by the surface areas as anticipated.

To quantify the outcomes, we compute the root mean square errors (RMSEs) of the state angles from $t = 30 - 100$ s (allowing 30 s for the robots to stabilize from their initial positions). The results are summarized in Table 2. It is evident that for the expected values of the damping coefficients ($A_d = 196$ cm^2, $A_t = 180$ cm^2) or higher, the angular errors were generally less than 10 deg in the simulation.

Overall, the simulation results corroborate that the introduced aerodynamic stabilizers bring about asymptotic stability, overcoming the large initial errors, as manifested by the Lyapunov analysis. This is without requiring any corrective maneuvers by the robots. The practical performance of the proposed framework for the vision-less cooperative transport task is next to be demonstrated.

Table 2. Experimental Conditions and RMSEs.

Experimental set	No. of robots	Payload mass [g]	Time [s]		⟨initial conditions⟩, equilibrium state, [RMSE] [deg]										
			from	to	α_0	β_0	α_1	β_1	ψ_1	α_2	β_2	ψ_2	α_3	β_3	ψ_3
Simulation without tails	3	161	0	0	⟨30⟩	⟨30⟩	⟨30⟩	⟨100⟩	⟨0⟩	⟨40⟩	⟨260⟩	⟨0⟩	-	-	-
			0	100	60	0	50	130	0	70	220	0	–	–	–
$A_d = 0\ cm^2$, $A_t = 0\ cm^2$			30	100	[18.9]	[43.6]	[18.1]	[36.5]	[0]	[14.6]	[44.4]	[0]	–	–	–
$A_d = 98\ cm^2$, $A_t = 0\ cm^2$			30	100	[7.2]	[10.9]	[9.2]	[13.8]	[0]	[7.7]	[19.3]	[0]	–	–	–
$A_d = 196\ cm^2$, $A_t = 0\ cm^2$			30	100	[3.4]	[7.8]	[7.9]	[7.1]	[0]	[4.6]	[13.6]	[0]	–	–	–
$A_d = 392\ cm^2$, $A_t = 0\ cm^2$			30	100	[2.5]	[5.1]	[5.4]	[5.8]	[0]	[3.2]	[8.6]	[0]	–	–	–
Simulation with tails	3	161	0	0	⟨30⟩	⟨30⟩	⟨30⟩	⟨100⟩	⟨60⟩	⟨40⟩	⟨260⟩	⟨−60⟩	–	–	–
			0	100	60	0	50	130	0	70	220	0	–	–	–
$A_d = 0\ cm^2$, $A_t = 0\ cm^2$			30	100	[22.8]	[37.5]	[34.5]	[81.5]	[60]	[21.4]	[72.5]	[60]	–	–	–
$A_d = 98\ cm^2$, $A_t = 90\ cm^2$			30	100	[5.5]	[13.3]	[11.8]	[12.9]	[1.5]	[8.1]	[22.8]	[1.5]	–	–	–
$A_d = 196\ cm^2$, $A_t = 180\ cm^2$			30	100	[3.0]	[6.9]	[6.2]	[7.9]	[0.5]	[5.4]	[11.9]	[0.5]	–	–	–
$A_d = 392\ cm^2$, $A_t = 360\ cm^2$			30	100	[1.8]	[4.7]	[3.9]	[4.5]	[0.3]	[2.6]	[5.9]	[0.3]	–	–	–
Single follower	1	111	0	5	⟨50⟩	⟨−30⟩	⟨50⟩	⟨150⟩	–	–	–	–	–	–	–
			5	50	60	0	60	180	–	–	–	–	–	–	–
Without damper			20	50	[4.9]	[17.8]	[5.7]	[14.6]	–	–	–	–	–	–	–
With damper			20	50	[3.8]	[12.5]	[3.6]	[8.2]	–	–	–	–	–	–	–
Leader–payload–follower	2	111	0	35	60	0	60	180	–	–	–	–	–	–	–
			35	70	45	0	45	180	–	–	–	–	–	–	–
			70	100	70	0	70	180	–	–	–	–	–	–	–
			0	100	[4.9]	[10.2]	[5.0]	[10.5]	–	–	–	–	–	–	–
Three–robot	3	161	0	35	45	0	45	135	–	45	225	–	–	–	–
			35	70	60	0	60	120	–	60	240	–	–	–	–
			70	100	45	0	45	135	–	45	210	–	–	–	–
			0	100	[4.7]	[6.7]	[5.9]	[9.2]	–	[5.4]	[9.4]	–	–	–	–
Disturbance rejection	3	161	0	120	45	0	45	135	–	45	225	–	–	–	–
Open–space with two robots	2	111	0	40	45	0	45	180	–	–	–	–	–	–	–
Open–space with four robots	4	211	0	25	45	0	45	80	0	45	180	0	45	280	0
Outdoor	3	161	0	70	45	0	45	135	0	45	225	0	–	–	–

5.4. Indoor Flight Experiments

Experiments were performed to assess the proposed passive strategy with the use of MoCap data to systematically validate the outcomes (during the flight, MoCap was only used for controlling the leader robot). However, the limited tracking volume of the arena only allows the case of $\nu_p = 0$ to be assessed. This subsequently rules out the use of tail dampers as the corrective torque in Equation (20) is dependent on $\|\nu_p\|$. Therefore, the yaw angles were directly controlled to be constant using the IMU feedback. This is achieved by minimizing the yaw rate and the integrated yaw rate provided by the gyroscope. The effectiveness of the payload dampers can still be comprehensively investigated. In this section, we conducted four sets of experiments to confirm the stabilizing effects of the payload dampers. This includes the disturbance rejection flight to show the robustness of the passive method as the system stabilizes to a different equilibrium state in the presence of errors or disturbances, as suggested by the inverse problem.

5.4.1. Single Follower and a Suspended Payload with and Without Payload Damper

To testify the effectiveness of the dampers attached beneath the payload, as suggested by Equation (17), a benchmark experiment was first conducted. Here, the leader robot was replaced with a fixed structure to eliminate the possible acceleration of the leader. Two sets of flights, one with and one without the payload dampers, were tested. In each set, a follower was employed, and the robot was first controlled with MoCap feedback to hover at the initial position. Then, at $t = 5$ s, the position feedback was cut off, and the follower was commanded to keep a constant thrust vector using the IMU measurements. The setpoint attitude and thrust magnitude in this phase, computed by Equations (12) and (13), corresponds to the equilibrium state that differs from the initial position, as indicated in Table 2.

Five repeated flights in each set, with and without the dampers, were trialed, and the results are presented in **Figure 3**a (one flight shown in Movie S2, Supporting Information). From the

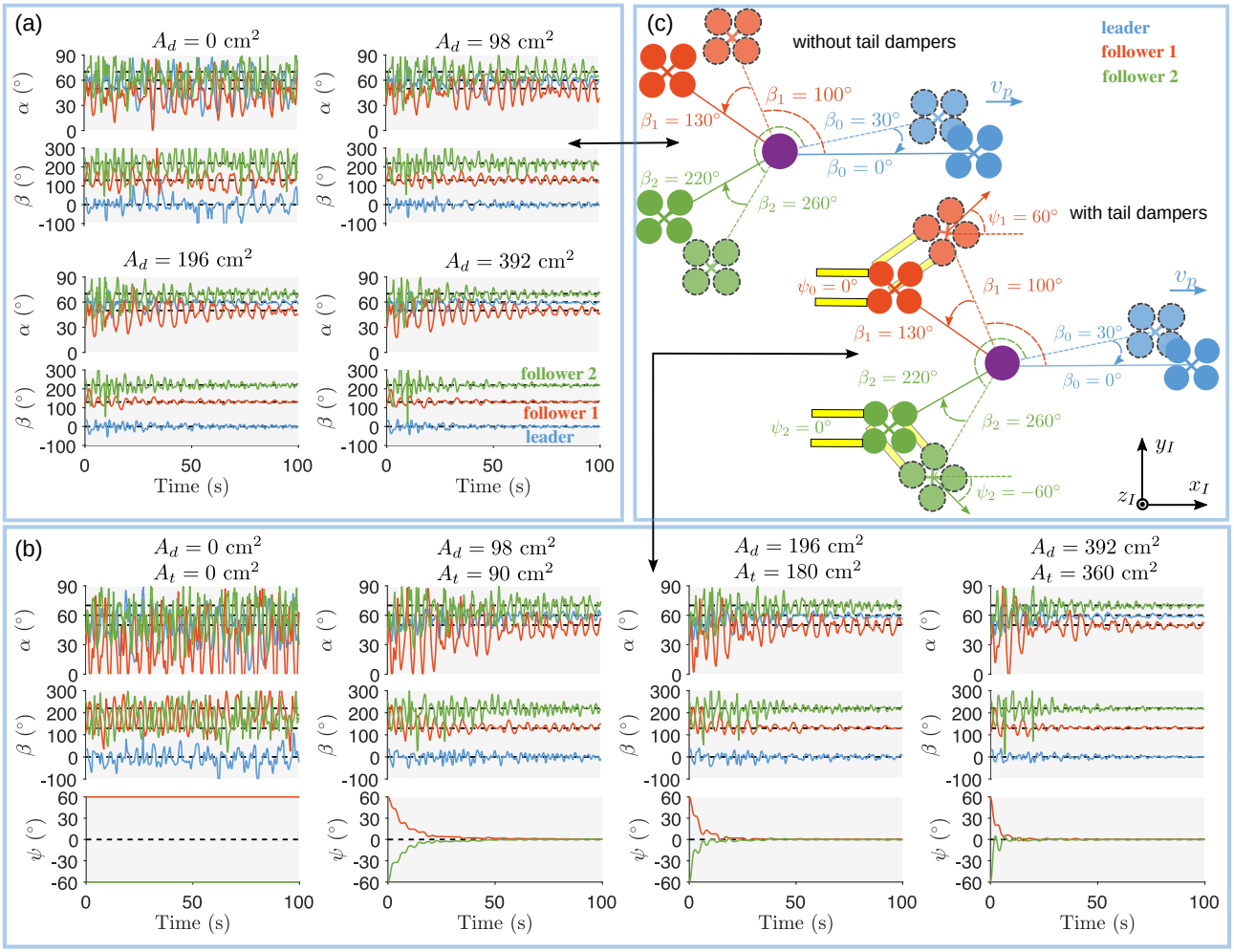

Figure 2. Simulation results with different sets of damping coefficients. The initial states for the two sets of simulations are identical in terms of elevation angles α_i and azimuth β_i. a) The trajectory results without tail dampers. b) The trajectory results with the tail dampers. c) Diagram showing the initial states and equilibrium states. The outcomes show that by the payload and tail dampers stabilize the system to the equilibrium state determined by the thrust vectors of the followers.

plots, it can be seen that the amplitudes of the oscillation reduced over time in both cases, but the follower with the dampers was quicker to stabilize to the equilibrium state, with visibly less oscillation around the setpoint after 10 s. The small stabilizing effect on the baseline set is attributable to the damping brought by the robot's body and spinning propellers. The RMSEs shown in Table 2 (computed from $t = 20 - 50$ s) suggest an approximate 30% reduction in the angular errors when the dampers were introduced. These flights testify the effectiveness of the payload dampers in passively stabilizing the payload and the follower through aerodynamic forces.

5.4.2. Leader-Payload-Follower Flights

In this set of flights, one leader and one follower cooperatively carried a payload, as captured in Figure 3b and Movie S3, Supporting Information. The 111 g payload was tied to the stabilizer. The leader was commanded to hover for the first 20 s while the follower maintained the setpoint angles listed in Table 2. The leader then slowly tracked a rectangular trajectory with varying altitudes (from 1.5 to 1.8 m) for 80 s. This slow movement involves unmodeled acceleration and can be perceived as disturbances when ν_p remains nominally zero. To further demonstrate the robustness, the flight was further divided into three phases with different angular setpoints (realized by altering the thrust vectors of the followers). As listed in Table 2, α_0 and α_1 were changed from 60° to 45° at $t = 35$ s and to 70° at $t = 70$ s. In other words, the angular setpoints were altered while the robots were slowly traveling.

With five flights performed, the consolidated results are shown in Figure 3b,c. Despite the occasional violation of the $\nu_p = 0$ condition when the leader traveled slowly and the setpoint angles were adjusted, the trajectory plots reveal overall satisfactory tracking performance. Although some oscillation of the payload and follower can be seen in Figure 5.4.1(b) due to the passive nature of the stabilizing mechanism (no feedforward correction), they tracked the reference closely and stably. In the generalized

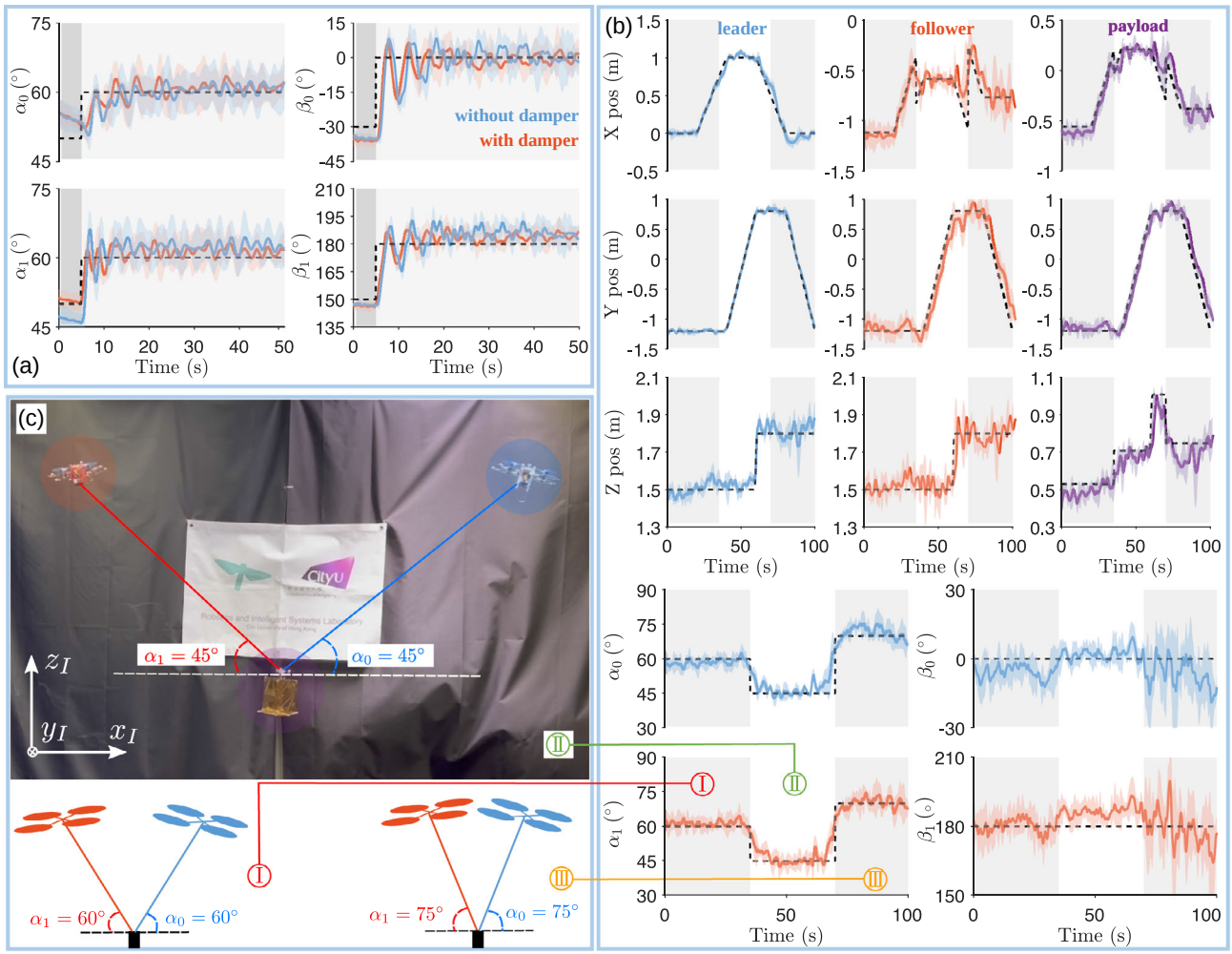

Figure 3. Flight results with one follower robot. a) Results of the test flights with a single-follower robot. The plots compare the elevation and azimuth angles from flights with (red) and without (blue) the payload stabilizer. Solid lines present the mean value from five flights, and the shades cover the range of one standard deviation. b) Trajectories of the leader (blue), follower (red), and payload (purple) in the form of cartesian position and elevation and azimuth angles. Black dashed lines are the references. Solid lines represent the means from five repeated flights. Shaded regions indicate the range of one standard deviation. Stabilized by the payload dampers, the flight underwent three different phases altered by the thrust vectors of the followers. c) Photographs and diagrams illustrate three equilibrium states. The leader (blue) and the follower (red) cooperatively carried a 111 g damper-attached payload. The cables are highlighted for visibility. Larger elevation angles result in a more compact configuration, suitable for transporting a payload in narrower spaces.

coordinates, the azimuth and elevation angles only deviated slightly from the setpoints. The larger errors of β_0 and β_1 after $t = 70$ s seen in Figure 3b do not indicate poor tracking performance as they are, in fact, caused by the singularity limit related to the definitions of the azimuth angles at high elevation angles. As α_0 and α_1 increase, position errors when projected onto the horizontal plane lead to amplified errors in β_0 and β_1. As presented in Table 2, the RMSEs of the elevation angles are only $\approx 5°$. The errors of the azimuth angles are somewhat larger ($\approx 10°$) owing to the projection issue, as explained.

5.4.3. Three-Robot Experiment

To further validate the effectiveness of the passive approach, we expanded the formation to involve three agents, resulting in one leader and two followers hoisting a 161 g payload, as depicted in **Figure 4**b and Movie S4, Supporting Information. At the beginning, the robots were set to hover for 20 s at the setpoints described in Table 2. Then, the trajectory for the leader was prescribed as a circle with a diameter of 1.0 m at a constant altitude from $t = 20$ to 100 s, covering a total distance of 3.2 m at an average speed of 0.04 m s^{-1}. The small speed and acceleration required for the circular path mean the assumption that $\nu_p = 0$ was slightly but persistently violated. Similar to the previous set of experiments, elevation and azimuth setpoints were adjusted twice during the flight by shifting the thrust vectors of the two followers, yielding three flight segments with different configurations shown in Figure 4b,c. The robots organized into a more compact formation from $t = 35$ to 70 s by raising the elevation angles.

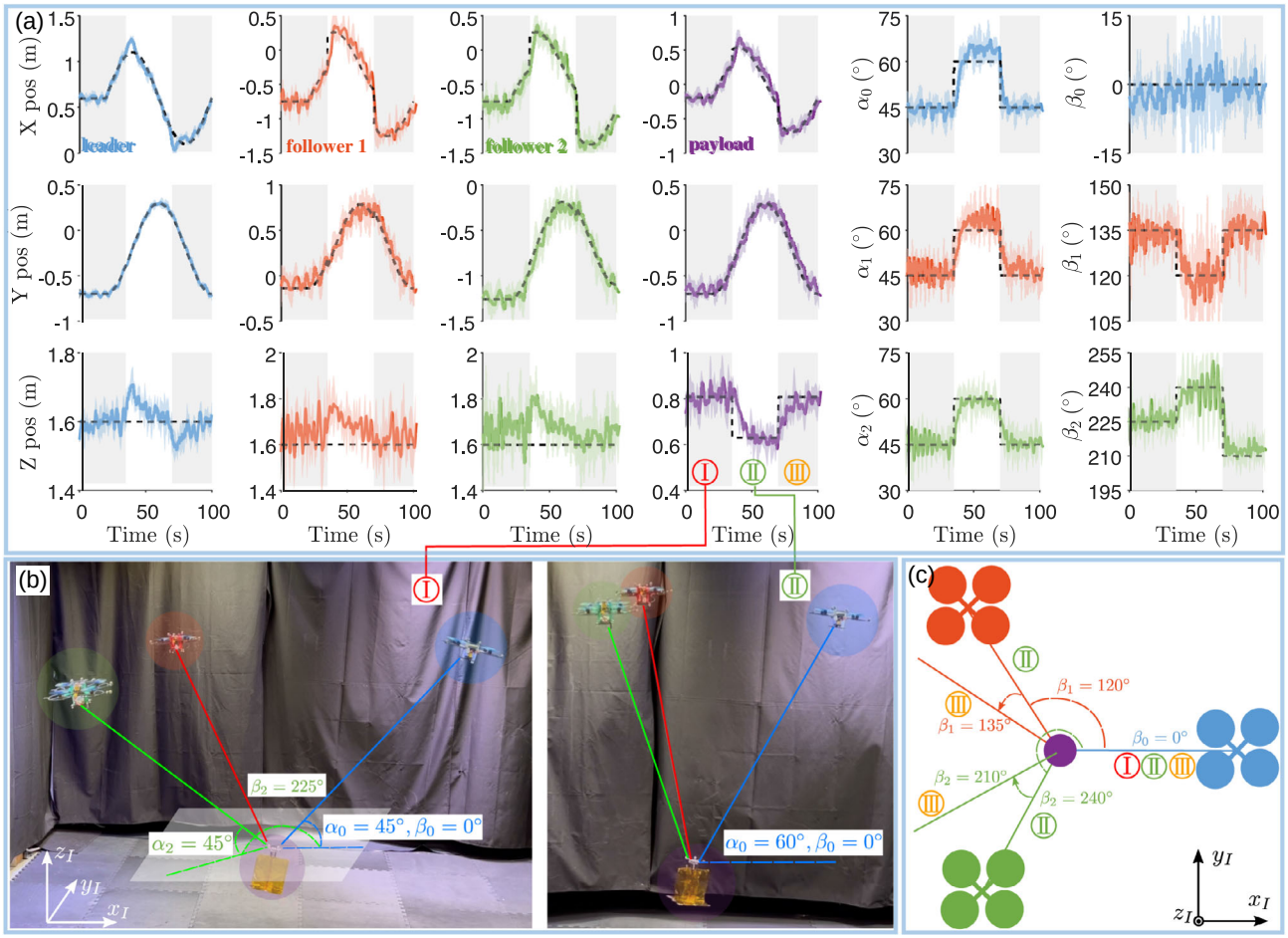

Figure 4. Indoor flight results with three robots. a) Trajectories of the leader (blue), follower 1 (red), follower 2 (green), and payload (purple) in three flight segments. Black dashed lines are the references. Solid lines represent the means from five repeated flights. Shaded regions indicate the range of one standard deviation. b) Snapshots of the three-robot experiment in phases I and II showing the leader (blue), follower 1 (red), and follower 2 (green) cooperatively transporting a 161-g payload (purple). The cables are highlighted for visibility. c) Schematic diagram highlighting different azimuth angles in three flight phases.

From five repeated flights, the payload dampers kept the system stable throughout, and the results are illustrated in Figure 4a. Qualitatively, the position plots suggest some degree of limited oscillation displayed by the payload and followers. Due to the symmetry, the behavior of the two followers was similar. A similar trend is observed for the angular states. As manifested by Figure 4a, the robots took a few seconds to stabilize after the changes of setpoint angles at $t = 35$ and 70 s. The RMSEs taken over five flights are found to be around 5° for the elevation angles and lower than 10° for the azimuth angles (Table 2). Compared to the single-follower flights earlier, the errors are of similar magnitude. The results display no noticeable decline in performance when the system is scaled up from two to three robots.

5.4.4. Robustness Against Disturbances

In addition to the minor violation of the zero flight speed condition previously tested, to further highlight the ability of the system to withstand and recover from external factors, a disturbance rejection test was carried out with two followers and a 161 g payload (see **Figure 5** and Movie S5, Supporting Information). The leader was instructed to hover in place, and the two followers realized the desired formation in Table 2.

As exemplified in Figure 5, disturbances were injected four times during the 120 s hovering flight. The first three occurrences were cable tucking at $t \approx 35, 45,$ and 65 s. These actions directly affected α_1, β_2, and β_1, respectively. After each disruption, the robots recovered from the push and stabilized to the equilibrium state within ≈ 3 s.

Thereafter, an electric fan (1 m away from the payload) was turned on from $t \approx 95 - 115$ s to inject wind disturbance. The maximum speed of the wind, as measured by an anemometer (Kanomax 6036-AG), reached 3.3 m s^{-1}. As depicted by Figure 5, the leader underwent relatively large fluctuations since the payload dampers were directly blown. The wind results in an oscillation of the system around a shifted equilibrium state with an evidently smaller α_0 and larger β_0. The observed behavior is consistent with the discussion on the inverse problem in Section 3 and the robustness analysis in Note S1, Supporting

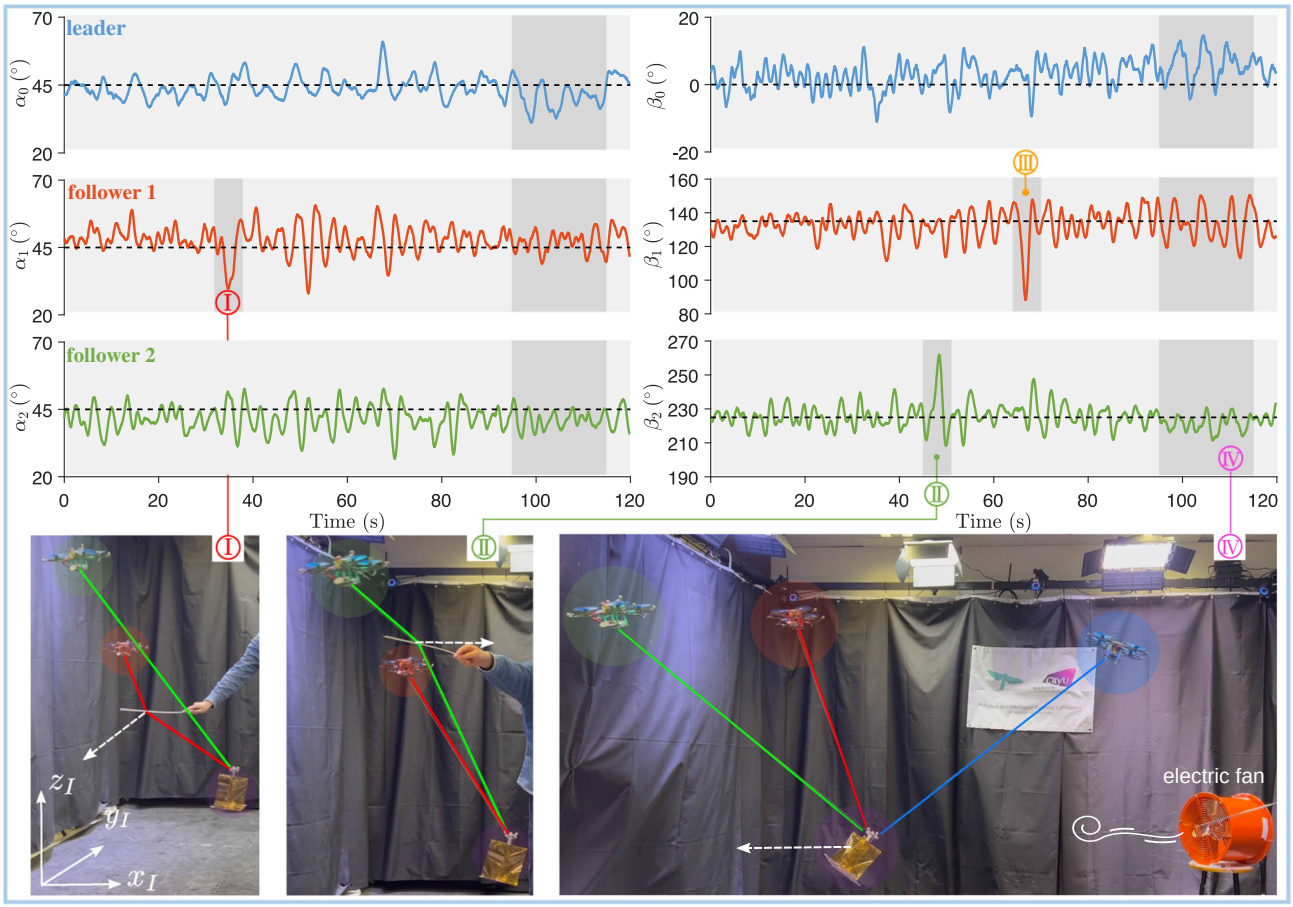

Figure 5. Tracking results of elevation and azimuth of the leader (blue), follower 1 (red), and follower 2 (green). Black dashed lines are the references. The formation underwent and recovered from four different disturbances (I–IV), in which I–III are cable tucking disturbances, with snapshots of I and II provided. In IV, the electric fan was turned on to inject wind disturbance, whose maximum speed reached 3.3 m s^{-1}. The white arrows represent the disturbance directions.

Information. In order to remain in equilibrium with $\nu_p = 0$, the leader must alter its thrust vector to compensate for the force induced by the wind on the payload dampers. This suggests a trade-off between the stabilizing effect of the damper's size and the sensitivity to wind disturbances. Despite the oscillation, the configuration of the formation was relatively stable and promptly recovered when the fan was turned off.

5.5. Flights in Open Space and Outdoors

While benefiting from the availability of MoCap feedback, the constraint on indoor space prevents the robots from maintaining a non-zero constant formation velocity νp. To testify the effectiveness of the tail dampers and demonstrate the transport of a payload over a long distance, flights in open and outdoor spaces were performed. In such settings, the robots may be subject to natural gusts, and the leader cannot rely on precise localization provided by the MoCap, rendering the cooperative transport task more realistic and challenging.

In the following experiments, the leader employed optical flow and ToF sensors to determine and control its velocity and altitude. The followers, like in previous tests, only depended on their IMUs to generate the desired collective thrust vector. However, the tail dampers were deployed to align the yaw angles of the followers with the intended travel directions. To do so, the proportional and integration terms in the yaw controller (integration of the yaw rate) were disabled, leaving only the rate term activated. In other words, the yaw orientation of each follower was dictated by the aerodynamic torque provided by their tail dampers.

5.5.1. Open-Space Flight with One Follower and Tail Dampers

The first test is designed to examine the contribution of the tail dampers mounted on the followers on their yaw orientations. The flight was conducted in a large passage inside a building without MoCap (Movie S6, Supporting Information). The test flight involves one follower. The speed and direction of the leader were regulated by the onboard feedback according to the command received by a human pilot. The leader was instructed to fly along an L-shaped trajectory covering a distance of over 20 m in $\approx$ 40 s, including a 90° turn, at the speed of 0.7 m s^{-1}. The elevation angles were 45° as provided in Table 2. To realize the L-shaped trajectory, we planned the state such that the follower robot retained the same pitch and roll angles during the

flight, and the change in the azimuth angle midflight was a result of the tail dampers-induced yaw rotation. Therefore, communication between the robots was not required.

Figure 6 illustrates the results. The composite image in Figure 6a shows the robots before and after the turn, whereas Figure 6b features the reconstruction of the trajectory. Note that only part of the flight (31 out of 40 s) can be reconstructed due to the limited coverage of the stereo cameras. It can be seen from Figure 6c that the leader executed a 90° turn at $t \approx 15$ s into the flight, sharply changing the traveling direction from $+\mathbf{e}_1$ to $-\mathbf{e}_2$ (or x_l to $-y_l$). It took approximately 10 s for the torque produced by the tail dampers on the follower to steer the robot into the new equilibrium angle. Despite the turn, the system remained stable the entire flight. The results demonstrate that (i) the tail dampers are effective in controlling the yaw angles of the follower as expected, and (ii) the leader can steer the system without any communication with the follower.

5.5.2. Open-Space Flight with Four Robots

To accommodate a heavier payload, four robots were recruited to carry a 211-g payload along a corridor within a building (**Figure 7** and Movie S7, Supporting Information). In this experiment, the configuration was chosen such that three robots provide forward force against the drag on the payload, as shown in Figure 7b and Table 2 (the azimuth angles are $\beta_1 = 80°$ and $\beta_3 = 280°$). Tail dampers were deployed on the followers to stabilize the traveling direction.

Four robots transported the payload over 20 m in 25 s in a straight line with an average speed of 0.8 m s^{-1}. Figure 7a presents the flight result as a composite image of the robots at $t = 1$ s and $t = 20$ s, with a snapshot at $t = 1$ s from a different perspective shown in Figure 7a. A short section of the flight trajectory (4 m out of 20) is reconstructed and illustrated in Figure 7d. This experiment demonstrates the feasibility and stability of multirobot flight with a heavy payload, even when there are many robots involved, as suggested by the stability analysis.

5.5.3. Outdoor Flight

Lastly, we realized a long-range payload transport with three robots hoisting a 161 g payload, as depicted in **Figure 8** and Movie S8, Supporting Information. In the outdoor environment, there existed natural gusts. The leader was remotely instructed by a human pilot to fly in a straight line, whereas the two followers were programmed to control their roll and pitch angles and the

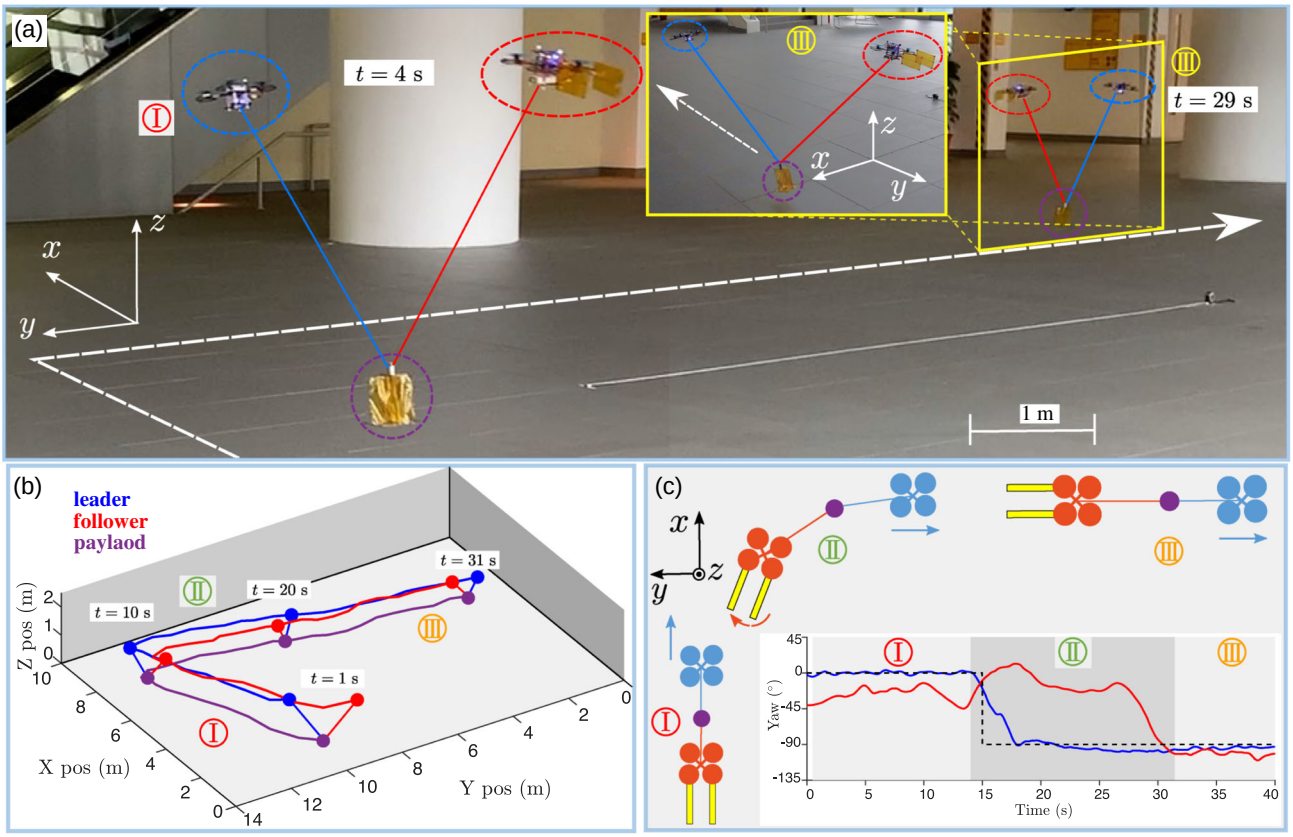

Figure 6. Open-space flight with one follower and tail dampers. a) Composite image of the flight in open space. The inset shows an alternative view at t =29 s. The transport of a 111 g payload (purple) along an L-shaped trajectory is realized with the leader (blue) and one follower (red). The path is divided into three parts: two straight sections I and III by a 90° turn. The turn is accomplished by changing the travel direction of the leader robot, whereas the follower is passively steered by the tail dampers (t =15–30 s, approximately). b) The outdoor trajectory is reconstructed by postprocessing (triangulation) two videos. Due to the limited field of view, only 30 s of the entire 40 s flight (over 20 m) can be reconstructed. c) Schematic drawing highlighting three phases in the trajectory distinguished by the traveling direction and the yaw orientation of the follower as influenced by the tail dampers.

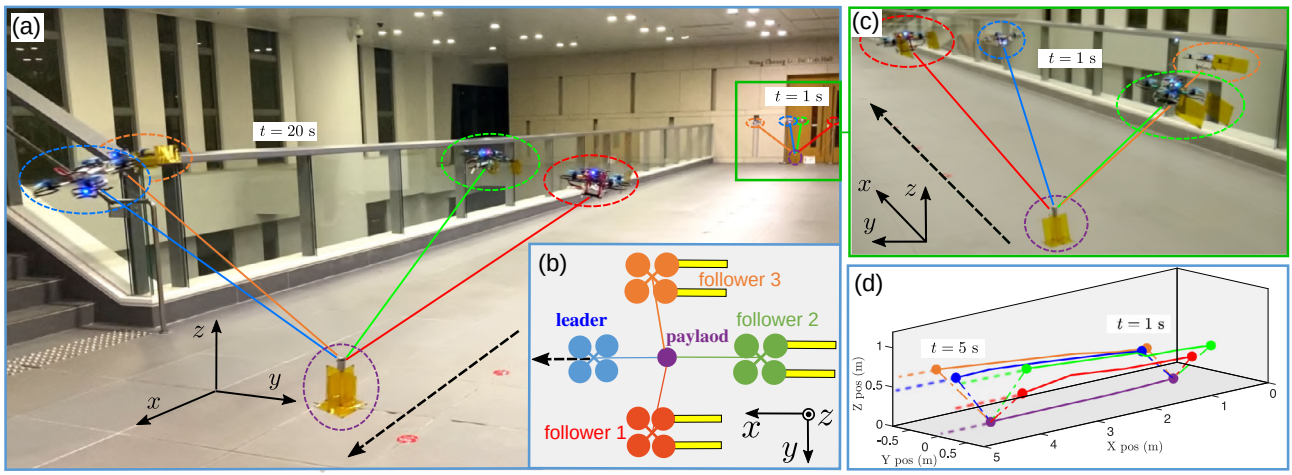

Figure 7. Open space flight with four robots. The robots carry a 211 g payload over 20 m in 25 s. a) Composite image of the formation at $t = 1$ s and $t = 20$ s. b) Top view of the configuration. c) Snapshot of the robots at $t = 1$ s from the rear. d) Part of the trajectory is reconstructed by postprocessing (triangulation) two videos. Due to the limited field of view, only 5 s of the entire 25 s flight can be reconstructed.

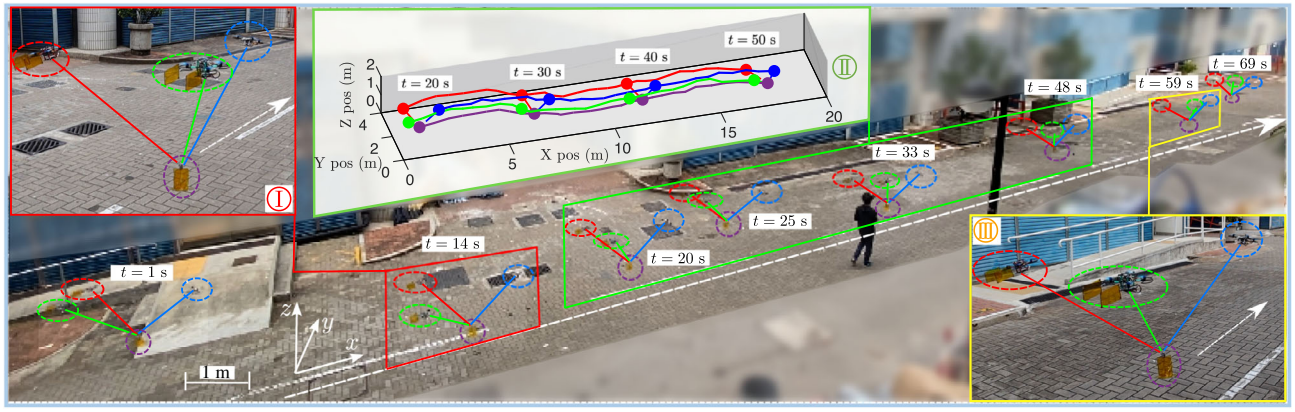

Figure 8. Composite image showing a 161 g payload (purple) being cooperatively transported by the leader (blue), follower 1 (red), and follower 2 (green). Two insets in red and yellow show photos captured from different locations at t =14 and 59 s, respectively. The trajectory is triangulated from two videos, showing only a 30 s section in the middle of the entire flight, from t =20 to 50 s, due to the limited field of view. The entire flight covered 45 m in 70 s.

thrust magnitudes according to the setpoints listed in Table 2. The tail dampers were deployed to stabilize the heading direction of the followers. Due to the substantial weight of the payload, the leader had to maintain a pitch angle of almost 30° to generate sufficient forward force.

Figure 8 presents two snapshots at $t = 14$ and 59 s and the partial trajectory generated from two camera views ($t \approx$20–50 s). Due to the limited field of view, only approximately 20 m of the 45 m flight could be reconstructed. It can be seen that the formation remained stable during the 70 s flight, despite the presence of some wind disturbances. The robots safely and robustly transported the payload over 45 m in 70 s at an average speed of 0.65 m s^{-1}. The combination of payload and tail dampers radically simplifies the sensing and control strategy for the follower robots by making the multiagent system inherently stable.

6. Conclusion and Discussion

In this paper, we proposed a mechanical strategy to passively stabilize a group of aerial robots for the transport of a suspended point-mass payload. Rather than relying on vision-based or traditional positioning methods, as seen in Table 1, which require additional hardware to meet the computational demand, we leveraged the passive dynamics to mechanically stabilize the system of multiple robots and the payload. Through the analysis of the dynamics, we showed that the aerodynamic damping induced by mechanical stabilizers is adequate for the robots to maintain the desired formation. With the leader robot responsible for navigating to the intended direction, the control of the follower robots is radically simplified to the regulation of only roll, pitch, and net thrust, requiring no communication even for changing the flight direction or speed. This method can

be generalized to any larger number of $n+1$ robots. The passive stabilization is independent of the number of follower robots, allowing the group to accommodate a heavier payload as practically possible while considering the physical limit and collision risks.

Through a series of flight experiments with two, three, and four robots, the passive framework has been shown to be effective in transporting a point-mass payload. We verified that the strategy is robust against disturbances. Although the assumption of a constant traveling velocity was imposed in the formulation of the stability analysis, the robots were able to deal with a tight turn. In the outdoor demonstration with three robots, the 45 m distance traveled is notably further than previous aerial transports of a suspended payload with onboard feedback. For instance, in the pioneering work,[32] two robots transported a payload over a distance of 3.3 m in 8 s using vision and tags. In ref. [33], three robots carried a rigid body payload over a distance of 31 m in 35 s in an indoor flight arena using vision-based coordinated control and interagent communication. It can be seen that the accomplishment herein rivals these state-of-the-art solutions but with the simplicity of the passive method. Furthermore, this passive strategy is, in principle, compatible with any number of the follower robots as long as it is physically viable; we have demonstrated this by a 20 m open-space flight with four robots and a heavier payload. However, the current development is still limited to the transport of a point mass payload, where the orientation of the payload is not taken into consideration. In the outdoor experiment, three robots carried the payload at the average collective speed of $0.7\,\mathrm{m\,s^{-1}}$, lower than the speed of three cooperative robots, which is $0.9\,\mathrm{m\,s^{-1}}$, as shown in ref.[33] and much lower than the maximum speed of $4.2\,\mathrm{m\,s^{-1}}$ achieved in ref.[19] by a team of two robots. High-speed and agile maneuvers remain challenging and inefficient for aerodynamic-based stabilization as the robots need to overcome additional air drag. The lack of feedforward actions also makes it difficult for the robots to actively compensate for non-zero acceleration.

The proposed passively stabilizing method based on lightweight, aerodynamic dampers is particularly suitable for small robots, such as those in refs. [36-39]. This is because the inertial force scales with ℓ^3 and the aerodynamic damping with the surface area or ℓ^2, where ℓ is the characteristic length. Hence, for small robots, the aerodynamic damping is significant or dominant over the inertial force, facilitating the stabilization of the system. Conversely, for large robots or heavier payloads, the inertial force prevails over the aerodynamic damping. Thus, the passive approach of employing mechanical stabilizers to generate aerodynamic damping is more effective for lightweight robots and payloads.

Overall, the mechanical solution eliminates the need for communication and sophisticated computation of vision-based approaches, replacing cameras and companion computers with 6.7 g air dampers. The framework is highly attractive for smaller aerial vehicles with constrained payload capacity. Furthermore, despite the inherent differences, we believe the two frameworks, namely, the use of passive dynamics and vision-based estimation and control methods are, in fact, complementary. It is foreseeable that the two methods can be used in conjunction or side-by-side as a backup mechanism. The integration of the two approaches is a possible research avenue for future works.

Supporting Information

Supporting Information is available from the Wiley Online Library or from the author.

Acknowledgements

This work was supported in part by the Research Grants Council of the Hong Kong Special Administrative Region of China under (grant no. CityU 11218022) and in part by the Shenzhen- Hong Kong-Macau Science and Technology Project (Category C) under (grant no. SGDX20220530111401009). The authors would like to thank J.X., T.W., B.P., and S.Y. for their assistance in carrying out flight experiments.

Conflict of Interest

The authors declare no conflict of interest.

Data Availability Statement

The data that support the findings of this study are available from the corresponding author upon reasonable request.

Keywords

aerial robots, aerodynamic damping, cooperative transport, passive stability, suspended payload

Received: March 1, 2023
Revised: April 20, 2023
Published online: June 22, 2023

[1] Y. Liu, J. M. Montenbruck, D. Zelazo, M. Odelga, S. Rajappa, H. H. Bülthoff, F. Allgöwer, A. Zell, *IEEE Trans. Rob.* **2018**, *34*, 870.
[2] A. Loquercio, E. Kaufmann, R. Ranftl, A. Dosovitskiy, V. Koltun, D. Scaramuzza, *IEEE Trans. Rob.* **2019**, *36*, 1.
[3] K. McGuire, C. De Wagter, K. Tuyls, H. Kappen, G. C. de Croon, *Sci. Rob.* **2019**, *4*, eaaw9710.
[4] E. Soria, F. Schiano, D. Floreano, *IEEE Rob. Autom. Lett.* **2021**, *7*, 73.
[5] W. Tabib, K. Goel, J. Yao, C. Boirum, N. Michael, *IEEE Trans. Rob.* **2021**, *38*, 1016.
[6] K. Bodie, M. Brunner, M. Pantic, S. Walser, P. Pfändler, U. Angst, R. Siegwart, J. Nieto, *IEEE Trans. Rob.* **2020**, *37*, 709.
[7] A. A. Paranjape, S.-J. Chung, K. Kim, D. H. Shim, *IEEE Trans. Rob.* **2018**, *34*, 901.
[8] S.-J. Chung, A. A. Paranjape, P. Dames, S. Shen, V. Kumar, *IEEE Trans. Rob.* **2018**, *34*, 837.
[9] A. Ollero, M. Tognon, A. Suarez, D. Lee, A. Franchi, *IEEE Trans. Rob.* **2021**, *38*, 626.
[10] A. Jiménez-Cano, D. Sanalitro, M. Tognon, A. Franchi, J. Cortés, *J. Intell. Rob. Syst.* **2022**, *105*, 68.
[11] H. Ando, Y. Ambe, A. Ishii, M. Konyo, K. Tadakuma, S. Maruyama, S. Tadokoro, *IEEE Rob. Autom. Lett.* **2018**, *3*, 1128.
[12] J. Thomas, G. Loianno, J. Polin, K. Sreenath, V. Kumar, *Bioinspiration Biomimetics* **2014**, *9*, 025010.
[13] B. Mu, P. Chirarattananon, *IEEE Trans. Rob.* **2019**, *36*, 458.

[14] F. Schiano, P. M. Kornatowski, L. Cencetti, D. Floreano, *IEEE Rob. Autom. Lett.* **2022**, *7*, 12 150.
[15] K. Sreenath, N. Michael, V. Kumar, in *2013 IEEE Int. Conf. Robotics and Automation*, IEEE, Piscataway, NJ **2013**, pp. 4888–4895.
[16] B. Xian, S. Yang, *IEEE/ASME Trans. Mechatron.* **2020**, *26*, 2653.
[17] K. Karydis, V. Kumar, *Interface Focus* **2017**, *7*, 20160088.
[18] L. Bauersfeld, D. Scaramuzza, *IEEE Rob. Autom. Lett.* **2022**, *7*, 2953.
[19] G. Loianno, V. Kumar, *IEEE Rob. Autom. Lett.* **2017**, *3*, 680.
[20] A. Tagliabue, M. Kamel, R. Siegwart, J. Nieto, *Int. J. Rob. Res.* **2019**, *38*, 1020.
[21] K. Oishi, T. Jimbo, in *2021 IEEE/RSJ Int. Conf. Intelligent Robots and Systems (IROS)*, IEEE, Piscataway, NJ **2021**, pp. 6322–6328.
[22] N. Michael, S. Kim, J. Fink, V. Kumar, in *Int. Design Engineering Technical Conf. and Computers and Information in Engineering Conf.*, Vol. *49040*, San Diego, CA **2009**, pp. 83–91.
[23] J. Fink, N. Michael, S. Kim, V. Kumar, *Int. J. Rob. Res.* **2011**, *30*, 324.
[24] Q. Jiang, V. Kumar, *IEEE Trans. Rob.* **2012**, *29*, 136.
[25] K. Sreenath, V. Kumar, *Robotics: Sci. Syst. IX* **2013**, *1*, r3.
[26] C. Meissen, K. Klausen, M. Arcak, T. I. Fossen, A. Packard, *IFAC-PapersOnLine* **2017**, *50*, 13150.
[27] B. E. Jackson, T. A. Howell, K. Shah, M. Schwager, Z. Manchester, *IEEE Rob. Autom. Lett.* **2020**, *5*, 3368.
[28] K. Mohammadi, S. Sirouspour, A. Grivani, *IEEE/ASME Trans. Mechatron.* **2020**, *25*, 1709.
[29] J. Geng, J. W. Langelaan, *J. Guidance Control Dyn.* **2020**, *43*, 1313.
[30] D. S. D'antonio, G. A. Cardona, D. Saldaña, *IEEE Rob. Autom. Lett.* **2021**, *6*, 3857.
[31] K. Mohammadi, S. Sirouspour, A. Grivani, *IEEE/ASME Trans. Mechatron.* **2021**, *27*, 2390.
[32] M. Gassner, T. Cieslewski, D. Scaramuzza, in *2017 IEEE Int. Conf. on Robotics and Automation (ICRA)*, IEEE, Piscataway, NJ **2017**, pp. 5196–5202.
[33] G. Li, R. Ge, G. Loianno, *IEEE Rob. Autom. Lett.* **2021**, *6*, 5316.
[34] H. Xie, X. Cai, P. Chirarattananon, in *2020 IEEE/RSJ Int. Conf. on Intelligent Robots and Systems (IROS)*, IEEE, Piscataway, NJ **2020**, pp. 1215–1221.
[35] H. Xie, K. Dong, P. Chirarattananon, *IEEE Access* **2022**, *10*, 81764.
[36] M. J. Anderson, J. G. Sullivan, T. K. Horiuchi, S. B. Fuller, T. L. Daniel, *Bioinspiration Biomimetics* **2020**, *16*, 026002.
[37] Z. E. Teoh, S. B. Fuller, P. Chirarattananon, N. Prez-Arancibia, J. D. Greenberg, R. J. Wood, in *2012 IEEE/RSJ Int. Conf. on Intelligent Robots and Systems*, IEEE, Piscataway, NJ **2012**, pp. 3209–3216.
[38] S. B. Fuller, Z. E. Teoh, P. Chirarattananon, N. O. Pérez-Arancibia, J. Greenberg, R. J. Wood, *Auton. Rob.* **2017**, *41*, 1555.
[39] N. J. Kohut, D. Zarrouk, K. C. Peterson, R. S. Fearing, in *2013 IEEE/RSJ Int. Conf. on Intelligent Robots and Systems*, IEEE, Piscataway, NJ **2013**, pp. 5593–5599.
[40] J. Norby, J. Y. Li, C. Selby, A. Patel, A. M. Johnson, *IEEE Trans. Rob.* **2021**, *37*, 1144.
[41] D. W. Haldane, K. C. Peterson, F. L. G. Bermudez, R. S. Fearing, in *2013 IEEE Int. Conf. on Robotics and Automation*, IEEE, Piscataway, NJ **2013**, pp. 3279–3286.
[42] A. L. Thomas, G. K. Taylor, *J. Theoretical Biol.* **2001**, *212*, 399.
[43] S. Bai, Q. He, P. Chirarattananon, *Sci. Rob.* **2022**, *7*, eabg5913.
[44] M. Piccoli, M. Yim, in *2015 IEEE Int. Conf. on Robotics and Automation (ICRA)*, IEEE, Piscataway, NJ **2015**, pp. 1716–1721.
[45] A. Bouman, P. Nadan, M. Anderson, D. Pastor, J. Izraelevitz, J. Burdick, B. Kennedy, in *2020 IEEE International Conference on Robotics and Automation (ICRA)*, IEEE, Piscataway, NJ **2020**, pp. 8511.
[46] M. Sitti, *Extreme Mech. Lett.* **2021**, *46*, 101340.
[47] D. Floreano, R. J. Wood, *Nature* **2015**, *521*, 460.
[48] S. Fuller, Z. Yu, Y. P. Talwekar, *Sci. Rob.* **2022**, *7*, eabq8184.
[49] K. Elamvazhuthi, Z. Kakish, A. Shirsat, S. Berman, *IEEE Trans. Rob.* **2020**, *37*, 418.
[50] S. Bai, R. Ding, P. Chirarattananon, *IEEE Rob. Autom. Let.* **2022**, *7*, 4016.
[51] R. Cory, R. Tedrake, in *AIAA Guidance, Navigation and Control Conf. and Exhibit*, Honolulu, Hawaii **2008**, p. 7256.
[52] N. Michael, J. Fink, V. Kumar, *Auton. Rob.* **2011**, *30*(1), 73.
[53] R. Ding, Y.-H. Hsiao, H. Jia, S. Bai, P. Chirarattananon, *IEEE Rob. Autom. Lett.* **2022**, *7*, 1581.
[54] X. Zhang, F. Zhang, P. Huang, J. Gao, H. Yu, C. Pei, Y. Zhang, *IEEE Rob. Autom. Lett.* **2021**, *6*, 1559.
[55] K. Klausen, C. Meissen, T. I. Fossen, M. Arcak, T. A. Johansen, *IEEE Trans. Control Syst. Technol.* **2018**, *28*, 653.
[56] R. Ritz, R. D'Andrea, in *2013 IEEE/RSJ Int. Conf. Intelligent Robots and Systems*, IEEE, Piscataway, NJ **2013**, pp. 3465–3471.
[57] X. Liang, Z. Zhang, H. Yu, Y. Wang, Y. Fang, J. Han, *IEEE/ASME Trans. Mechatron.* **2022**, *27sss*, 5159.